Crystallographic analysis of fatigue fracture initiation in 8Ni-0.1C martensitic steel

AUTHOR(S):

Okada, Kazuho; Shibata, Akinobu; Takeda, Yasunari; Tsuji, Nobuhiro

CITATION:

Okada, Kazuho ...[et al]. Crystallographic analysis of fatigue fracture initiation in 8Ni-0.1C martensitic steel. International Journal of Fatigue 2021, 143: 105921.

ISSUE DATE:

2021-02

URL:

http://hdl.handle.net/2433/277477

International Journal of Fatigue 143 (2021) 105921

Contents lists available at ScienceDirect

International Journal of Fatigue

journal homepage: www.elsevier.com/locate/ijfatigue

Crystallographic analysis of fatigue fracture initiation in 8Ni-0.1C martensitic steel

Kazuho Okada[a,*], Akinobu Shibata[a,b,c], Yasunari Takeda[a], Nobuhiro Tsuji[a,b]

[a] Department of Materials Science and Engineering, Kyoto University, Yoshida-honmachi, Sakyo-ku, Kyoto 606-8501, Japan
[b] Elements Strategy Initiative for Structural Materials (ESISM), Kyoto University, Yoshida-honmachi, Sakyo-ku, Kyoto 606-8501, Japan
[c] Research Center for Structural Materials, National Institute for Materials Science (NIMS), 1-2-1 Sengen, Tsukuba 305-0047, Japan

ARTICLE INFO

Keywords:
Fatigue fracture
Martensitic steel
Electron backscattering diffraction
Crystallographic orientation analysis

ABSTRACT

The present paper investigated characteristics of fatigue fracture behavior, particularly initiation stage of fatigue fracture (Stage I), in an as-quenched martensitic steel from microstructural and crystallographic points of view. The detailed crystallographic orientation analysis using EBSD revealed that block boundaries in lath martensite structure were the most preferential initiation sites for fatigue cracks. We found that incompatibility of plastic strains between adjacent blocks was the origin for the formation of initial fatigue cracks at block boundaries. Moreover, plastic deformation along {0 1 1} slip planes also played an important role on the transgranular crack propagation.

1. Introduction

High strength steels are widely used in buildings, bridges, railways, and other structures. One of the major concerns for structural materials is “fatigue fracture”, which occurs under alternating loads. Fatigue fracture leads to unexpected serious accidents, so that preventing the fatigue fracture of high strength steels is a very important technological challenge.

It has been recognized that fatigue fracture process under a constant amplitude loading can be divided into four stages; Stage I, Stage II_a, Stage II_b, and Stage II_c [1,2]. Stage I is the initiation of fatigue cracks. The most significant factor in Stage I is the irreversible slips which are caused by repetitive shear stresses [3–5]. Stage II corresponds to the crack propagation and final rupture. In Stage II_a, the crack propagation direction changes into perpendicular to the loading axis. In Stage II_b, the cracks propagate perpendicular to the loading axis and the resultant fracture surfaces consist of striations. Stage II_c is the final rupture and the fracture mode is ductile or brittle or their mixtures [1]. Especially in a low loading amplitude condition, Stage I and Stage II_a occupy a large part of entire fatigue life and they are the most complex stages of fatigue fracture [1,6]. Although these stages have been extensively studied in various kinds of metals and alloys [3–5,7–9], the details are still unclear.

Lath martensite structure is a typical microstructure in high-strength low- and medium-carbon steels. It is well known that lath martensite satisfies Kurdjumov-Sachs (K-S) orientation relationship with respect to austenite, given by $\{111\}_A//\{011\}_M$, $\langle 101\rangle_A//\langle 111\rangle_M$, where the subscripts A and M denote austenite and martensite, respectively. In the K-S orientation relationship, there are twenty-four equivalent crystallographic variants that are transformed from a single grain of austenite. Table 1 presents the twenty-four variants in the K-S orientation relationship [10–12]. Due to the existence of such crystallographic variants, transformation to lath martensite divides an austenite grain into several structural units with different length scales, i.e., lath, sub-block, block, and packet [10,13,14]. A martensite lath is a single crystal of martensite with a thickness of about 0.2 μm. Misorientation between adjacent laths is less than 5° [11]. A sub-block is an aggregation of laths with an identical variant. A block comprises a specific combination of two variants with a small misorientation, for example V1-V4, V2-V5, V3-V6 in Table 1. Boundaries between adjacent laths (i.e., habit planes) or adjacent blocks correspond to the identical crystallographic planes of approximately parallel to {0 1 1} that satisfies the parallel plane relationship in the K-S orientation relationship [10–12]. It has been proposed that block boundaries have the largest contribution to the strength of lath martensite structures [15,16]. A packet consists of six variants (V1 to V6, V7 to V12, V13 to V18, or V19 to V24 in Table 1) that have the same parallel plane relationship in the K-S orientation relationship. Usually several packets appear within each prior austenite grain. Because crystallographic orientations of martensite variants are different to each other, crystallographic analysis can

* Corresponding author.
E-mail address: okada.kazuho.56z@st.kyoto-u.ac.jp (K. Okada).

https://doi.org/10.1016/j.ijfatigue.2020.105921
Received 9 July 2020; Received in revised form 21 August 2020; Accepted 26 August 2020
Available online 26 September 2020

Table 1
The twenty-four crystallographic variants of martensite crystals in the K-S orientation relationship [10–12].

Variant No.	Plane parallel	Direction parallel	Misorientation angle from V1 (V7, V13, V19)	
V1	$(111)_A // (011)_M$	$[\bar{1}01]_A // [\bar{1}\bar{1}1]_M$	-	from V1
V2		$[\bar{1}01]_A // [\bar{1}1\bar{1}]_M$	60.00°	
V3		$[01\bar{1}]_A // [\bar{1}\bar{1}1]_M$	60.00°	
V4		$[01\bar{1}]_A // [\bar{1}1\bar{1}]_M$	10.53°	
V5		$[1\bar{1}0]_A // [\bar{1}\bar{1}1]_M$	60.00°	
V6		$[1\bar{1}0]_A // [\bar{1}1\bar{1}]_M$	49.47°	
V7	$(1\bar{1}1)_A // (011)_M$	$[10\bar{1}]_A // [\bar{1}\bar{1}1]_M$	49.47°	-
V8		$[10\bar{1}]_A // [\bar{1}1\bar{1}]_M$	10.53°	60.00°
V9		$[\bar{1}\bar{1}0]_A // [\bar{1}\bar{1}1]_M$	50.51°	60.00°
V10		$[\bar{1}\bar{1}0]_A // [\bar{1}1\bar{1}]_M$	50.51°	10.53°
V11		$[011]_A // [\bar{1}\bar{1}1]_M$	14.88°	60.00°
V12		$[011]_A // [\bar{1}1\bar{1}]_M$	57.21°	49.47°
V13	$(\bar{1}11)_A // (011)_M$	$[0\bar{1}1]_A // [\bar{1}\bar{1}1]_M$	14.88°	-
V14		$[0\bar{1}1]_A // [\bar{1}1\bar{1}]_M$	50.51°	60.00°
V15		$[\bar{1}0\bar{1}]_A // [\bar{1}\bar{1}1]_M$	57.21°	60.00°
V16		$[\bar{1}0\bar{1}]_A // [\bar{1}1\bar{1}]_M$	20.61°	10.53°
V17		$[110]_A // [\bar{1}\bar{1}1]_M$	51.73°	60.00°
V18		$[110]_A // [\bar{1}1\bar{1}]_M$	47.11°	49.47°
V19	$(11\bar{1})_A // (011)_M$	$[\bar{1}10]_A // [\bar{1}\bar{1}1]_M$	50.51°	-
V20		$[\bar{1}10]_A // [\bar{1}1\bar{1}]_M$	57.21°	60.00°
V21		$[0\bar{1}\bar{1}]_A // [\bar{1}\bar{1}1]_M$	20.61°	60.00°
V22		$[0\bar{1}\bar{1}]_A // [\bar{1}1\bar{1}]_M$	47.11°	10.53°
V23		$[101]_A // [\bar{1}\bar{1}1]_M$	57.21°	60.00°
V24		$[101]_A // [\bar{1}1\bar{1}]_M$	21.06°	49.47°

precisely characterize the lath martensite structure.

For understanding the underlying mechanism of fatigue fracture in high strength martensitic steels, it is very important to clarify the relationship between microstructure of lath martensite and fatigue fracture behavior, particularly fatigue crack initiation. However, this has not yet been accomplished. In this research, characteristics of the fatigue crack initiation behavior at Stage I in an as-quenched martensitic steel were experimentally investigated from microstructural and crystallographic points of view.

2. Experimental

An Fe-8Ni-0.1C alloy was used in the present study. The detailed chemical composition is presented in Table 2. A cast ingot of the alloy was homogenized at 1373 K for 32.4 ks (9 h) in vacuum, followed by water quenching. The homogenized plate was cold-rolled from 15 mm to 6 mm in thickness and then austenitized at 1273 K for 1.8 ks (0.5 h) in vacuum, followed by iced-brine quenching and sub-zero cooling in liquid nitrogen. The as-quenched specimen had a fully martensitic structure without pro-eutectoid ferrite. After the heat treatment, the specimens were mechanically ground down to a thickness of 5 mm in order to remove the decarburized layers formed during the heat treatment.

Table 2
Chemical composition of the alloy used in the present study (wt.%).

C	Si	Mn	P	S	Al	Ni	Fe
0.116	0.005	0.01	0.001	0.0015	0.033	7.94	Bal.

Rectangle bar-type tensile/fatigue test specimens with a gauge length of 10 mm and a width (and a thickness) of 5 mm were fabricated from the heat-treated specimens. The tensile/fatigue test specimens were polished electrolytically in a solution of 50 ml $HClO_4$ + 450 ml CH_3COOH before tests. Stress-controlled tensile-compression fatigue tests at ambient temperature were carried out by using a servo-hydraulic machine (Shimazu, SERVO EHF-EV101k1) with a stress ratio of -1 and a frequency of 10 Hz. The stress waveform was a sine wave. Uniaxial tensile tests at an initial strain rate of 8.3×10^{-4} s^{-1} were also performed at ambient temperature in air.

The initial microstructure of the heat-treated specimen was observed using optical microscopy and electron backscattering diffraction (EBSD) in a scanning electron microscope (JEOL: JSM-7100F) at an acceleration voltage of 15 kV. The specimens for the optical microscopy observation were etched in a 3% nital solution. Fracture surfaces of the fatigue-tested specimens were observed using scanning electron microscopy (SEM, JEOL: JSM-7800F). To study the microstructural and crystallographic features of the fatigue fracture behavior, crystal orientation mappings on the mid-thickness sections parallel to the loading axis of the fatigue-tested specimens were performed by EBSD. Ni layers with a thickness of approximately 100 μm were electrodeposited onto the fatigue-tested specimens to preserve the fracture surfaces. The electrodeposition solution was an aqueous solution of 150 g L^{-1} Ni_2SO_4 + 15 g L^{-1} H_3BO_4. The deposition was performed at ambient temperature and a current density of 100 A m^{-2} for 86.4 ks (24 h). One side of the electrodeposited specimen was mechanically polished until the specimen thickness became half of the initial thickness, and then

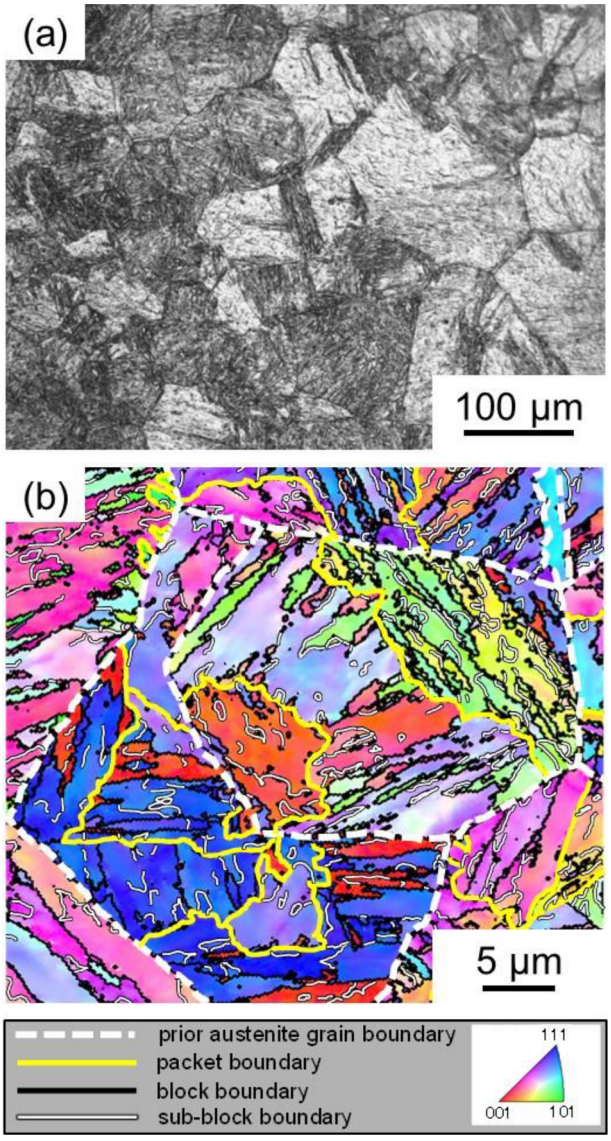

Fig. 1. (a) Optical microscopy image and (b) EBSD orientation map of the heat-treated specimen. The colors in the EBSD orientation map express the orientations parallel to the normal direction (ND) of the observed section and the stereographic triangle below the EBSD orientation map shows the correspondence between color and crystal orientation along ND.

electrolytically polished in the same solution as that used for the tensile/fatigue test specimen preparations. The EBSD measurements and analyses were performed with the TSL OIM Data Collection program and the TSL OIM Analysis program, respectively. In the EBSD orientation maps, positions of sub-block boundaries, block boundaries, packet boundaries, and prior austenite grain boundaries in lath martensite structure were identified by crystallographic orientation analysis based on the method reported by Morito et al. [11,12] and Kitahara et al. [17]. In addition, the microstructures around micro-cracks and fracture surfaces were observed by backscattering electron (BSE) images using a SEM (JEOL: JSM-7800F).

3. Results and discussion

3.1. Initial microstructure and mechanical properties

Fig. 1 shows (a) an optical microscopy image and (b) an EBSD orientation map of the heat-treated specimen (the colors in the EBSD orientation map express the orientations parallel to the normal

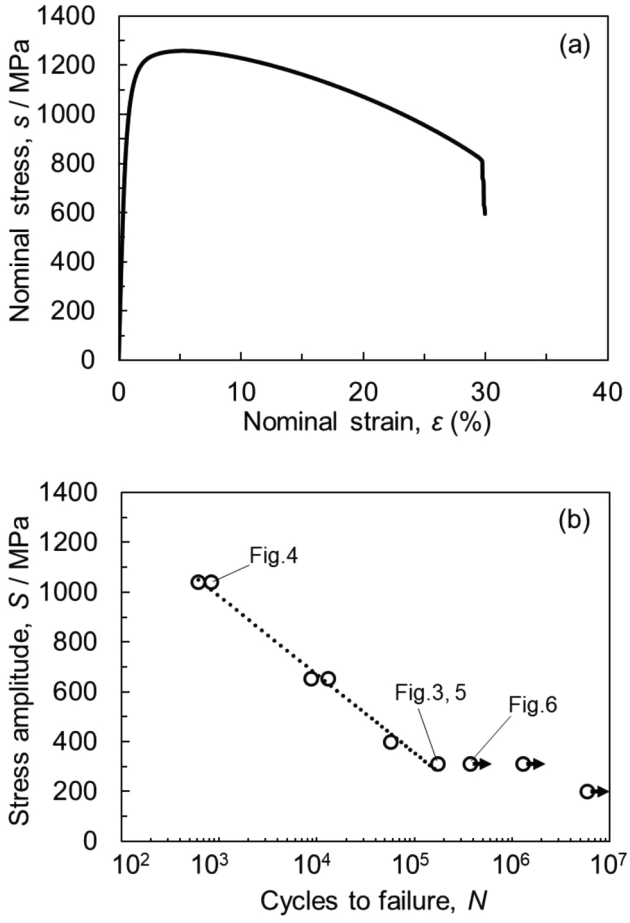

Fig. 2. (a) Nominal stress – nominal strain curve obtained from the uniaxial tensile test, and (b) S-N plot from the fatigue tests. The arrow marks indicate unbroken specimens.

direction (ND) of the observed section and the stereographic triangle below the EBSD orientation map shows the correspondence between color and crystal orientation along ND). In the EBSD orientation map of Fig. 1(b), the positions of sub-block boundaries, block boundaries, packet boundaries, and prior austenite grain boundaries are indicated by white solid lines with black rim, black solid lines, yellow solid lines, and white broken lines, respectively. In the following EBSD orientation maps, the positions of these boundaries are represented in the same way. The microstructure exhibited a typical lath martensite structure consisting of sub-blocks, blocks, and packets inside each prior austenite grain. The average sizes of blocks, packets, and prior austenite grains measured by a line interception method were 2.2 μm, 18.5 μm, and 56 μm, respectively.

Fig. 2 shows (a) a nominal stress - nominal strain curve of the uniaxial tensile test and (b) a relationship between stress amplitude and number of cycles to failure (S-N plot) in the fatigue tests. In the S-N plot, the arrow marks indicate unbroken specimens. According to Fig. 2(a), the tensile strength and the 0.2% proof stress were 1259 MPa and 967 MPa, respectively. Assuming that the fatigue limit is the stress amplitude under which fatigue fracture did not occure after 10^6 cycles, the fatigue limit of the specimen was about 200 MPa.

3.2. Observation of fracture surface

The fracture surfaces of the tensile-tested specimens were fully covered with dimples. This indicates that the specimen was fractured in a ductile manner. In the fatigue-tested specimens, on the other hand, the morphology of fracture surface changed with the progress of the

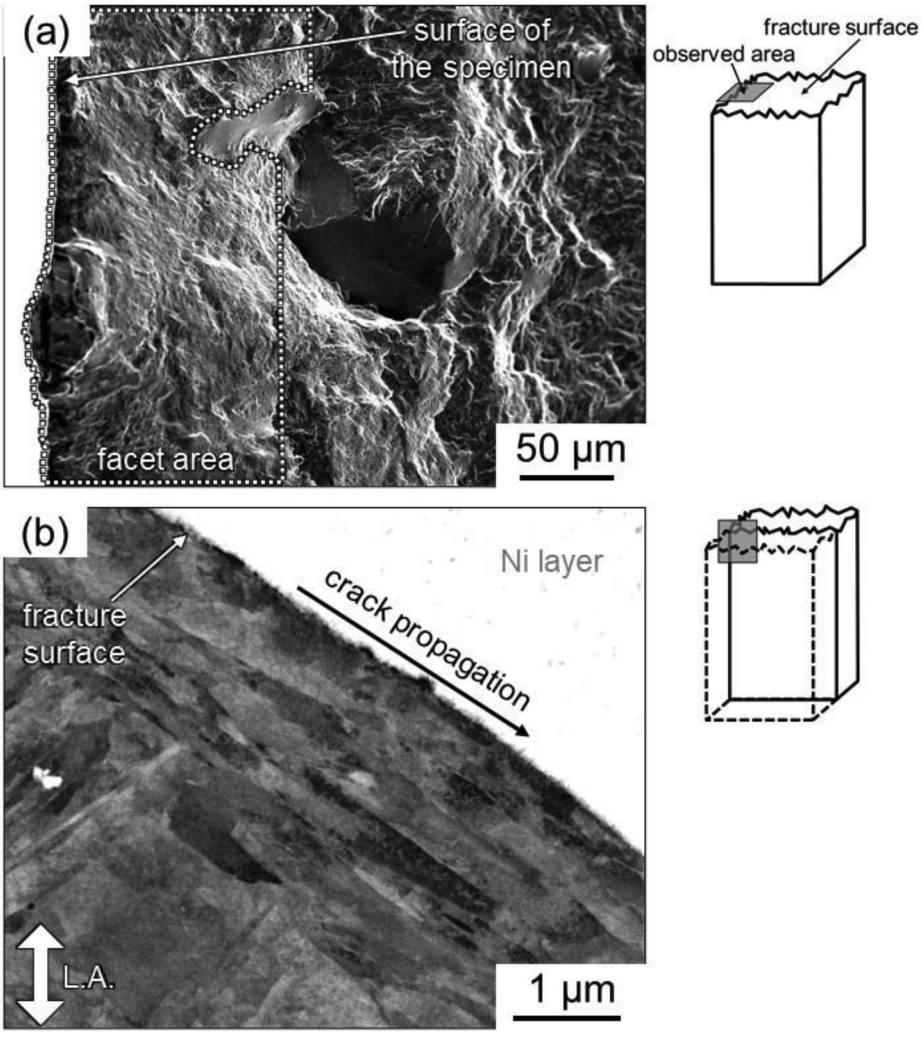

Fig. 3. (a) SEM image showing the fracture surface and (b) SEM-BSE image showing the microstructure near the fracture surface of the fatigue-fractured specimen after the fatigue test (S = 311 MPa, N = 1.7 × 10^5). The loading axis is indicated as L.A. in (b).

fracture. Fig. 3 shows (a) an SEM image of the fracture surface and (b) an SEM-BSE image showing the microstructure on the mid-thickness section around the fracture surface after the fatigue test (S = 311 MPa, N = 1.7 × 10^5). The observed areas are schematically illustrated at the right side of Fig. 3. The white area of Fig. 3(b) is the Ni layer electrodeposited to preserve the fracture surface. The fracture surface consists of a facetted area (surrounded by a dotted line) and a small amount of intergranular-like surface (Fig. 3(a)). The facet size was as large as two or three prior austenite grains. The existence of the facet with similar size was also reported as a feature of Stage I in some papers [18,19]. Usually, transmission electron microscopy has been used to observe lath structures. As shown in Fig. 3(b), however, we can clearly observe lath structures by electron channeling contrast using SEM-BSE. Because the initiation part of the fracture surface at Stage I was nearly parallel to the lath plane, we can suppose that the fatigue cracks were initiated at lath boundaries, sub-block boundaries, or block boundaries. Similar morphologies of the fracture surface in the region of Stage I were confirmed regardless of the stress amplitude.

3.3. Crystallographic features of fatigue crack initiation

Characteristics of the initiation of fatigue crack were analyzed using EBSD orientation mappings. Fig. 4 presents (a) an SEM image and (b) a corresponding EBSD orientation map showing the specimen surface after the fatigue test (S = 1039 MPa, N = 824). Before conducting the EBSD measurement, the specimen surface was slightly polished with a 0.02 μm colloidal silica suspension to remove the surface roughness formed by the fatigue test. Several cracks are visible in the SEM image of Fig. 4(a), and the positions of these cracks are indicated by thick black solid lines in the EBSD orientation map of Fig. 4(b). Using the several EBSD orientation maps in different areas, we statistically analyzed the relationship between crack initiation sites and lath martensite structure. The total number of cracks analyzed was 87. Fig. 4(c) is a histogram showing the relative proportion of cracks initiated at each type of boundaries in the lath martensite structure. For the cracks existed inside blocks, it was very difficult to identify whether they formed on sub-block/lath boundaries or not. Accordingly, these are classified as cracks initiated “inside block” in Fig. 4(c). Because more than 60 % of the observed cracks were initiated at block boundaries, we can conclude that block boundaries are the most preferential initiation sites of fatigue cracks in the as-quenched martensitic steel.

Fig. 5 shows (a, c) SEM-BSE images and (b, d) corresponding EBSD orientation maps of the areas on the mid-thickness section near the side surface of the specimen after the fatigue test (S = 311 MPa, N = 1.7 × 10^5). The observed areas in Fig. 5(a–d) were located within a given prior austenite grain. The light gray areas in the SEM-BSE images and the black areas in the EBSD orientation maps correspond to the electrodeposited Ni layers. The surfaces in Fig. 5(a, b) were fairly flat. No block/packet/prior austenite grain boundaries connected to the surface. In addition, clear extrusions/intrusions could not be recognized

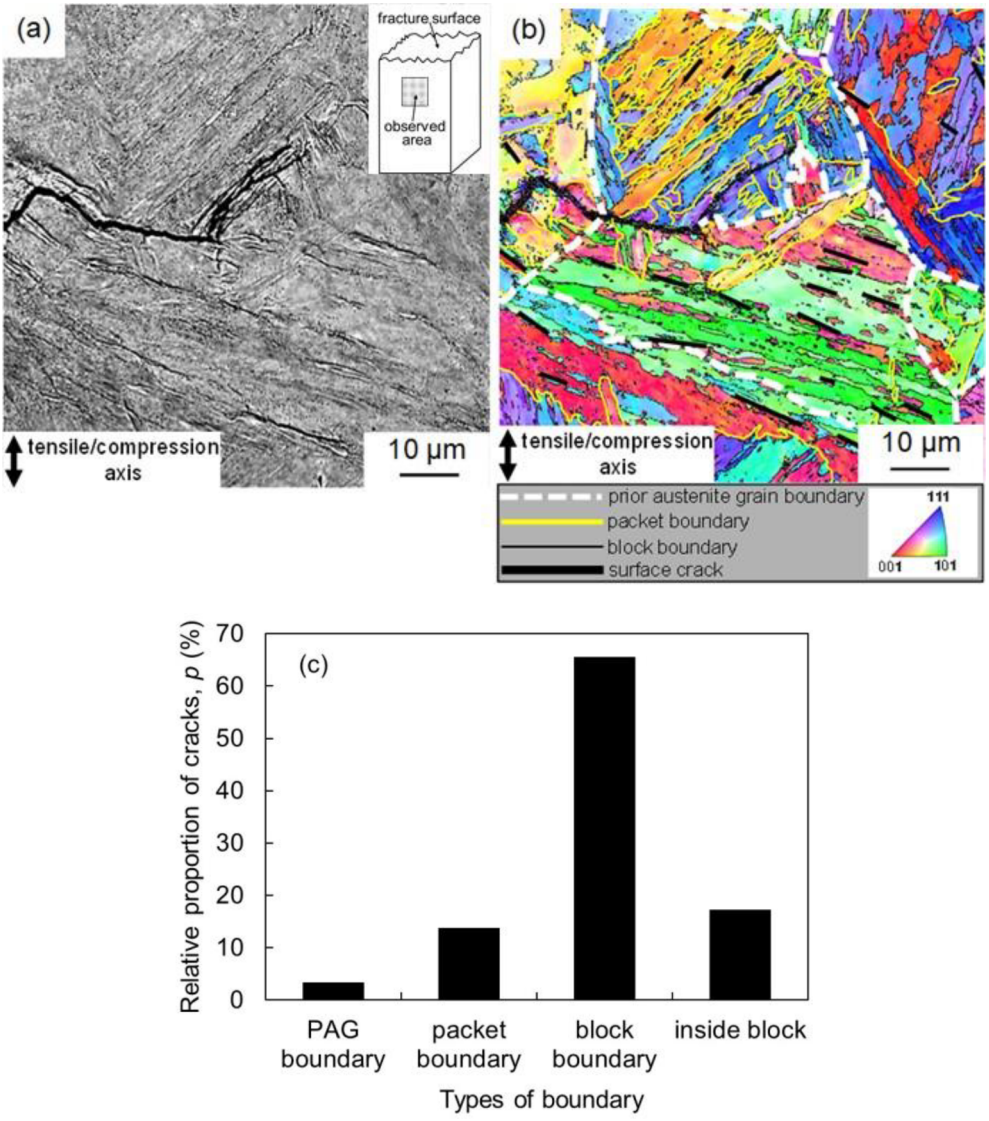

Fig. 4. (a) SEM image and (b) corresponding EBSD orientation map showing the specimen surface after the fatigue test (S = 1039 MPa, N = 824). (c) The relative proportion of cracks initiated at each type of boundaries in the lath martensite structure (S = 1039 MPa, N = 824).

at the positions where the sub-block boundaries between V7 and V10 connected to the surface. In contrast, several extrusions/intrusions were observed in the region shown in Fig. 5(c). It was clear from Fig. 5(d) that these extrusions/intrusions formed along block boundaries. In particular, large extrusion/intrusion formed along the block boundary between V2 and V6 as indicated by a white arrow. One can easily imagine that these extrusions/intrusions would develop to the initial cracks of fatigue fracture. We note that these extrusions/intrusions were clearly introduced by alternating loads and the surface roughness was not due to macroscopic plastic deformation. This is because the stress amplitude of the specimen observed in Fig. 5 was 311 MPa which is much smaller than the 0.2% proof stress (967 MPa).

In order to discuss the formation mechanism of the extrusions/intrusions, we analyzed the plastic deformation behavior of the martensite variants in Fig. 5(b, d). Nambu et al. [20] and Michiuchi et al. [21] reported that, at strain levels below 8% in tensile deformation, “in-lath-plane slip systems”, i.e., the slip systems having Burgers vectors parallel to the habit planes of laths, with large Schmidt factors were preferentially activated, even when the Schmidt factors of “out-of-lath-plane slip systems”, i.e., the slip systems having Burgers vectors not parallel to the habit planes of laths, were larger than those of the “in-lath-plane slip systems”. Although typical slip planes in body-centered cubic (BCC) crystals are {0 1 1}, {1 1 2}, and {1 2 3}, Schastlivtsev et al. [22] suggested that the primary slip planes in the as-quenched low-carbon martensitic steels were {0 1 1} and {1 1 2}. On this basis, we focused on {0 1 1} ⟨1 1 1⟩ and {1 1 2} ⟨1 1 1⟩ slip systems whose slip directions were parallel to the habit planes of laths. Because the habit plane of laths corresponds to {0 1 1} which satisfies the parallel plane relationship in the K-S orientation relationship, the habit plane of each martensite variant corresponds to (0 1 1) plane based on the coordinate system of each martensite variant, as shown in Table 1. For a given martensite variant, two kinds of ⟨1 1 1⟩ slip directions, i.e., [−1 −1 1] and [1 −1 1], are parallel to the habit plane of laths, and the possible slip planes for [−1 −1 1] slip directions are (0 1 1), (1 0 1), (1 −1 0), (1 1 2), (−1 2 1), and (2 −1 1), while those for [1 −1 1] slip direction are (0 1 1), (1 1 0), (1 0 −1), (1 2 1), (−1 1 2), and (2 1 −1). As a result, there are twelve “in-lath-plane slip systems” for each martensite variant. We can identify all the “in-lath plane slip systems” for each martensite variant through the crystallographic orientation analysis using EBSD orientation maps of Fig. 5(b, d). Table 3 shows values of the maximum Schmidt factors for the “in-lath-plane slip systems” in each variant in Fig. 5. Because the slip amounts might be different between {0 1 1} ⟨1 1 1⟩ and {1 1 2} ⟨1 1 1⟩ slip systems even if the Schmidt factors are the same, we summarized the Schmidt factors of these two slip

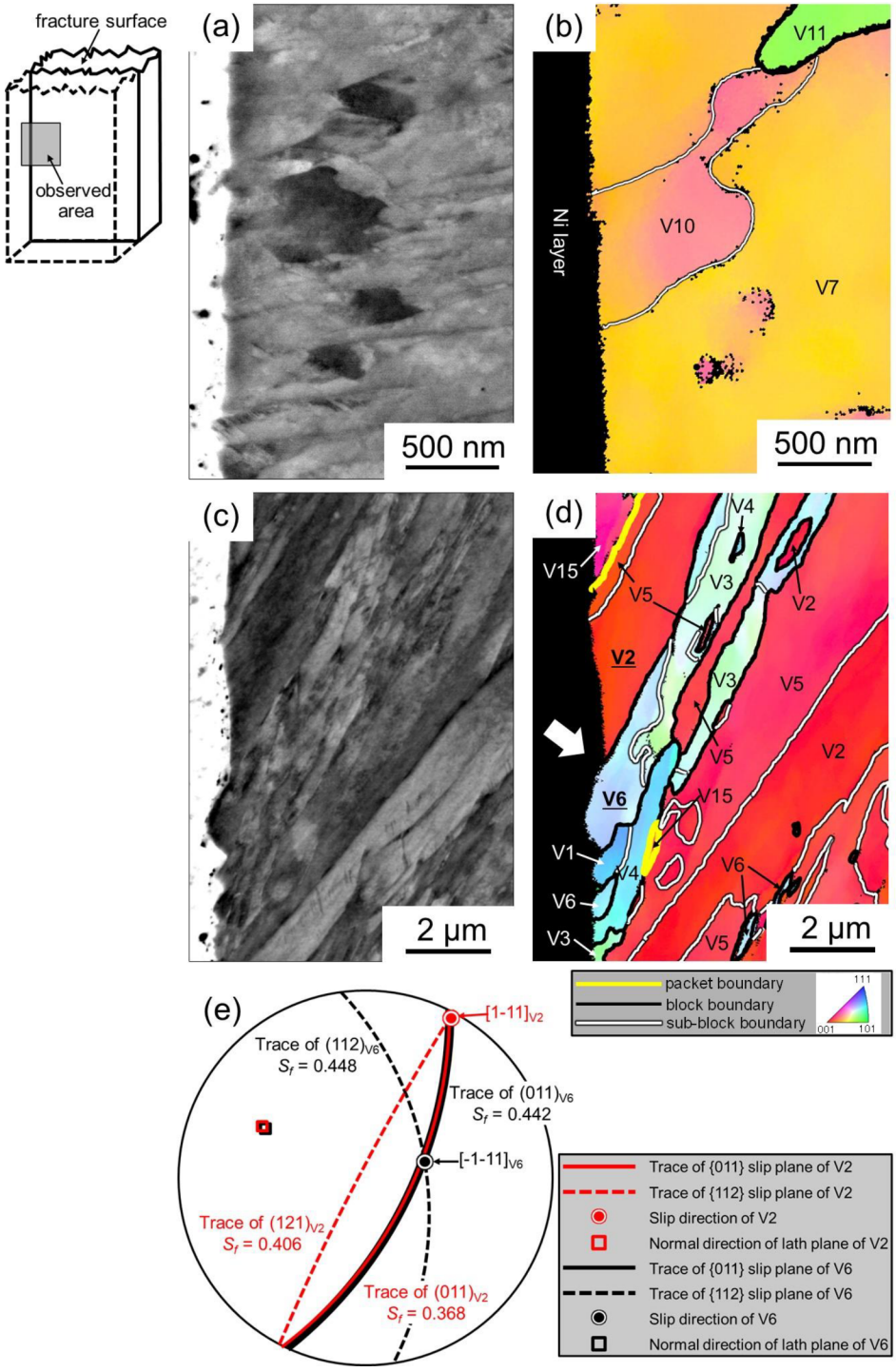

Fig. 5. (a), (c) SEM-BSE images and (b), (d) corresponding EBSD orientation maps of the areas on the mid-thickness section near the side surface of the specimen after the fatigue test (S = 311 MPa, N = 1.7 × 10^5). (e) Stereographic projection showing the slip systems with maximum Schmidt factors in V2 and V6.

systems separately. We found that the maximum Schmidt factor of {0 1 1} ⟨1 1 1⟩ slip systems in V6 (S_f = 0.442, (0 1 1) [−1 −1 1]) was much larger than that in V2 (S_f = 0.368, (0 1 1) [1 −1 1]), and the maximum Schmidt factor of {1 1 2} ⟨1 1 1⟩ slip systems in V6 (S_f = 0.448, (1 1 2) [-1–11]) was also larger than that in V2 (S_f = 0.406, (1 2 1) [1 −1 1]). Because it can be assumed that a larger Schmidt factor leads to a larger amount of plastic strain, the difference in the maximum Schmidt factors would cause an incompatibility of plastic strains at the block boundary between V2 and V6. The block boundaries between V1 and V6, V4 and V6, V3 and V4, the sub-block boundaries between V2 and V5, V7 and V10, and the packet boundary between V5 and V15 also connected to the specimen surface in Fig. 5(b, d). As summarized in Table 3, the difference in the maximum Schmidt factors of the possible slip systems between V1 and V6, V4 and V6, V3 and V4, V2 and V5, V5 and V15 were much smaller than those between V2 and V6. On the other hand, the difference in the maximum Schmidt factors of the possible slip systems between V7 and V10 (sub-block boundary) were larger than those between V2 and V6. However, the values of the maximum Schmidt factors of the possible slip systems in V7 and V10 were much smaller than those in the other variants, as shown in

Table 3
The maximum Schmidt factors of "in-lath-plane slip systems" for each martensite variants existed in Fig. 5.

Variant No.	Maximum Schmidt factors of "in-lath-plane slip systems"	
	{011}⟨111⟩	{112}⟨111⟩
V1	0.458	0.428
V2	0.368	0.406
V3	0.433	0.441
V4	0.449	0.439
V5	0.387	0.411
V6	0.442	0.448
V7	0.331	0.368
V10	0.248	0.282
V15	0.344	0.387

Table 3. Considering that the stress amplitude of the fatigue test was 311 MPa, which was much smaller than the 0.2% proof stress of the material, we could infer that the amounts of plastic strain in V7 and V10 were notably smaller than those in the other variants. In addition, the slip directions with maximum Schmidt factors in V2 and V6 were different as shown in the stereographic projection (Fig. 5(e)). The difference in the operated slip directions would also cause an incompatibility of plastic strains at the block boundary between V2 and V6. Consequently, the incompatibility of plastic strains due to the difference in the maximum Schmidt factors and the slip directions is the origin for the formation of large extrusion/intrusion at the block boundary between V2 and V6.

Similar to the case of the block boundary between V2 and V6 shown in Fig. 5, large incompatibility of plastic strains would also arise at packet boundaries and prior austenite grain boundaries, depending on the location. Actually, some fatigue cracks were initiated at packet boundaries and prior austenite grain boundaries, as shown in Fig. 4. We consider that block boundaries are preferential initiation sites of the fatigue cracks, as shown in Fig. 4, due to the higher density of block boundaries compared with packet boundaries and prior austenite grain boundaries in lath martensite structure.

3.4. Crystallographic features of Stage I cracks

In order to investigate crystallographic features of the fatigue crack propagation in Stage I, the fatigue tests were stopped before the final rupture and areas around the main cracks were analyzed using EBSD orientation mappings. Fig. 6 shows (a) an SEM image and (b) an EBSD orientation map around the main crack on the mid-thickness section of the specimen after the fatigue test (S = 311 MPa, $N = 3.7 \times 10^5$). The area of the EBSD measurement shown in Fig. 6(b) is indicated by white broken rectangles in (a). The facets of the crack corresponding to block boundaries, packet boundaries, and prior austenite grain boundaries are indicated by black solid lines, yellow solid lines, and white broken lines, respectively, in the EBSD orientation map of Fig. 6(b). In addition, the red dotted lines represent traces of {011} planes nearly parallel to the facets of the crack. We found that the Stage I crack (left side of Fig. 6(b)) preferentially propagated along block boundaries. It should be noted that all of the facet components, which did not propagate along certain kinds of boundaries, were parallel to one of the six crystallographically equivalent {011} plane traces. Furthermore, the crack propagated preferentially along packet boundaries and prior austenite grain boundaries in the right side of Fig. 6(b). This feature was consistent with the fracture surface morphology shown in Fig. 3(a). We consider that the right side of Fig. 6(b), where the crack propagated along the packet boundaries and the prior austenite grain boundaries, was the Stage II_a crack.

Based on the results described above, we can conclude that the Stage I cracks, which were initiated mainly at block boundaries due to incompatibility of plastic strains between neighboring martensite

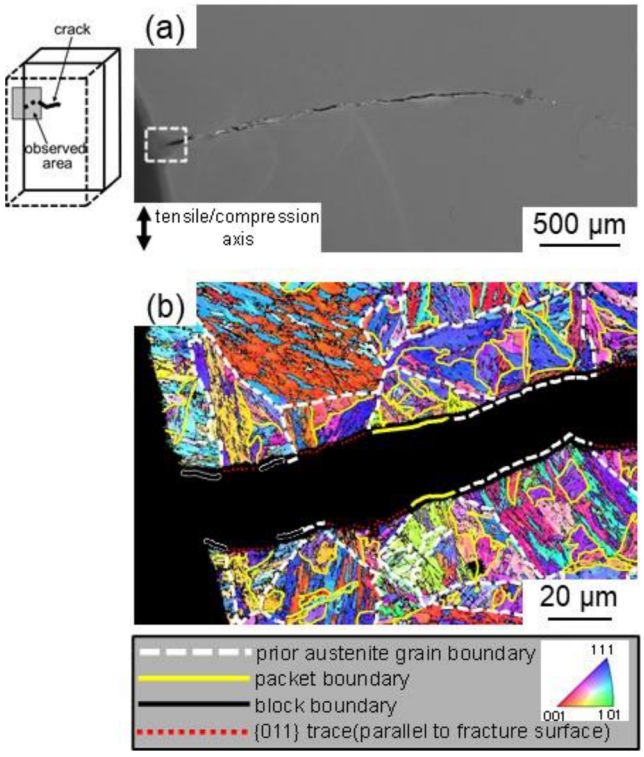

Fig. 6. (a) SEM image and (b) EBSD orientation map on the mid-thickness section around the main crack of the specimen after the fatigue test (S = 311 MPa, $N = 3.7 \times 10^5$). The observed area shown in (b) is indicated by white broken rectangle in (a).

variants, preferentially propagated along block boundaries. Moreover, all of the facet components, which did not correspond to any boundaries, were originated from the fracture propagated parallel to {011} crystallographic planes in a transgranular manner. Because {011} planes are slip planes in BCC crystal, we can suggest that plastic deformation along {011} slip planes also played an important role on the transgranular fatigue fracture in the martensitic steel.

4. Summary

We investigated the fatigue fracture behavior, particularly at the stage of fracture initiation (Stage I), of the as-quenched martensitic steel by means of the EBSD orientation analysis, and reached the following conclusions.

1. Among several kinds of boundaries in lath martensite structure, fatigue fracture was initiated mainly at block boundaries. The EBSD orientation analysis suggested that the initial fatigue cracks (extrusions/intrusions) along block boundaries were caused by plastic strain incompatibility between adjacent martensite blocks.
2. Through the EBSD orientation analysis, we found that the Stage I cracks mainly propagated along block boundaries. Moreover, the cracks sometimes deviated from the boundaries and propagated parellel to {011} planes in a transgranular manner. Because {011} planes were slip planes in BCC crystal, we could suggest that plastic deformation along {011} slip planes also played an important role on the transgranular fatigue fracture in the martensitic steel.

Declaration of Competing Interest

The authors declare that they have no known competing financial interests or personal relationships that could have appeared to influence the work reported in this paper.

Acknowledgement

This study was financially supported by JSPS KAKENHI Grant Number JP19J21267, JP15H04158, JP19H02459 and the Elements Strategy Initiative for Structural Materials (ESISM) from MEXT Japan.

References

[1] Kobayashi H. Fractography and fracture mechanics. J Soc Mater Sci Jpn 1980;29:198–203.
[2] Birlbeck G, Inckle AE, Waldron GWJ. Aspects of Stage II fatigue crack propagation in low-carbon steel. J Mater Sci 1971;6:319–23.
[3] Mughrabi H. Microstructural mechanisms of cyclic deformation, fatigue crack initiation and early crack growth. Philos Trans Royal Soc A 2015;373(2038).
[4] Risbet M, Feaugas X, Guillemer-Neel C, Clavel M. Use of atomic force microscopy to quantify slip irreversibility in a nickel-base superalloy. Scr Mater 2003;49:538.
[5] Fujisawa T, Hamada S, Koga N, Sasaki D, Tsuchiyama T, Nakada N, et al. Proposal for an engineering definition of a fatigue crack initiation unit for evaluating the fatigue limit on the basis of crystallographic analysis of pearlitic steel. Int J Fract 2014;185:17–29.
[6] Kobayashi H, Nakazawa H, Komine A. Fractographic study on Stage 1 crack propagation process. Trans JSME 1975;41:9–21.
[7] Polak J, Man J, Obrtlik K. AFM evidence of surface relief formation and models of fatigue crack nucleation. Int J Fatigue 2003;25:1027–36.
[8] Man J, Vystavel T, Weidner A, Kubena I, Petrenec M, Kruml T, et al. Study of cyclic strain localization and fatigue crack initiation using FIB technique. Int J Fatigue 2012;39:44–53.
[9] Polak J, Man J. Fatigue crack initiation – the role of point defects. Int J Fatigue 2014;65:18–27.
[10] Miyamoto G, Kaneshita T, Chiba T, Furuhara T. Crystallographic restriction in martensite and bainite transformations in steels. J Jpn Inst Metals Mater 2015;79:339–47.
[11] Morito S, Huang X, Furuhara T, Maki T, Hansen N. The morphology and crystallography of lath martensite in alloy steels. Acta Mater 2006;54:5323–32.
[12] Morito S, Tanaka H, Konishi R, Furuhara T, Maki T. The morphology and crystallography of lath martensite in Fe-C alloys. Acta Mater 2003;54:1789–99.
[13] Marder AR, Krauss G. The morphology of martensite in iron-carbon alloys. Trans Am Soc Metals 1967;60:651–60.
[14] Marder JM, Marder AR. The morphology of iron-nickel massive martensite. Trans Am Soc Metals 1969;62:1–10.
[15] Shibata A, Nagoshi T, Sone M, Morito S, Higo Y. Evaluation of the block boundary and sub-block boundary strengths of ferrous lath martensite using a micro-bending test. Mater Sci Eng, A 2010;527:7538–44.
[16] Morito S, Yoshida H, Maki T, Huang X. Effect of block size on the strength of lath martensite in low carbon steels. Mater Sci Eng, A 2006;438–440:237–40.
[17] Kitahara H, Ueji R, Tsuji N, Minamino Y. Crystallographic features of lath martensite in low-carbon steel. Acta Mater 2006;54:1279–88.
[18] Kitano T, Tagawa T, Aihara S, Miyata T. Influence of microstructures on fatigue crack initiation and propagation in low-carbon steel. TETSU-TO-HAGANE 1997;83:395–400.
[19] Asami K, Terasawa M. Study of early stage of fatigue crack in low carbon steel. J Soc Mater Sci Jpn 1981;30:803–8.
[20] Nambu S, Michiuchi M, Ishimoto Y, Asakura K, Inoue J, Koseki T. Transition in deformation behavior of martensitic steel during large deformation under uniaxial tensile loading. Scr Mater 2009;60:221–4.
[21] Michiuchi M, Nambu S, Ishimoto Y, Inoue J, Koseki T. Relationship between local deformation behavior and crystallographic features of as-quenched lath martensite during uniaxial tensile deformation. Acta Mater 2009;57:5283–91.
[22] Schastlivtsev VM, Rodionov DP, Khlebnikova YuV, Yakovleva IL. Peculiarity of structure and crystallography of plastic deformation of lath martensite in structural steels. Mater Sci Eng, A 1999;275:437–42.